


## PAPER

[View Article Online](#)  
[View Journal](#) | [View Issue](#)Cite this: *Dalton Trans.*, 2025, **54**, 11525

# Promoting electromagnetic wave absorption for conductive metal–organic frameworks through crystal morphology controlling†

Xueling Wang, Xuan Zhang, Jiaqi Lu and Zhiliang Liu \*

Conductive metal–organic frameworks (cMOFs) with  $\pi$ -d conjugation that can effectively promote the transport and migration of free electrons and improve electrical conductivity are considered as potential high-efficiency electromagnetic wave (EMW) absorption materials. However, the microstructural regulation of cMOFs with highly efficient EMW absorption remains a challenge due to the complexity of organic ligands and the uncontrollability of self-assembly reactions. Herein, two distinctly different microstructures or morphologies of Ni-TABQ cMOFs are synthesized by assembling the 2,3,5,6-tetraaminobenzoquinone (TABQ) ligands and  $\text{Ni}^{2+}$  ions through the manipulation of different reaction environments. The synergistic effect between the intrinsic conductivity and bulk microstructure of the obtained Ni-TABQ-1 optimizes electromagnetic parameters, displaying outstanding EMW absorption performance, with an  $\text{RL}_{\min}$  value of  $-62.68$  dB at 2.94 mm and an EAB of 5.12 GHz. These results demonstrate that the microstructural and conductivity control of cMOFs could offer an accessible and positive guide to developing superior EMW absorption materials.

Received 24th April 2025,  
Accepted 1st July 2025

DOI: 10.1039/d5dt00967g

[rsc.li/dalton](https://rsc.li/dalton)

## Introduction

Electromagnetic wave (EMW) absorption materials that possess the capability to transform electromagnetic energy into thermal or other forms of energy are becoming increasingly popular in functional coating materials<sup>1,2</sup> and are widely used in civilian technology and military fields, promising to solve the problem of electromagnetic pollution and realize radar stealth technology.<sup>3,4</sup> In general, the high performance of EMW absorption materials should satisfy the requirements of ideal impedance matching and strong attenuation capacity as much as possible. Meanwhile, the EMW absorption materials should also meet the qualities of thin thickness, light weight, good absorption capacity (reflection loss (RL)  $< -10$  dB), and effective absorption bandwidth (EAB, RL  $< -10$  dB frequency range).<sup>5,6</sup> Metal–organic frameworks (MOFs), which are crystal materials formed by self-assembly of bridging ligands and metal ions/clusters,<sup>7,8</sup> are among the most notable multifunctional materials. Particularly, composites derived from the pyrolysis products of MOF precursors have excellent advantages of EMW absorption properties by virtue of the characteristics, including a large specific surface area and a controllable chemical composition and microstructure.<sup>9</sup> Since the structure

or composition of the precursor may be destroyed during the pyrolysis process or dangerous gases resulting in secondary pollution may be produced, it is highly desired to develop novel MOF-based EMW absorption materials without any pyrolysis.

Conductive MOFs (cMOFs), as a new type of MOF with intrinsic electron conductivity, not only have the characteristics of traditional MOFs but also have amazing conductivity with intrinsic electron mobility, expecting to emerge as an outstanding EMW absorption material without requiring an extensive pyrolysis process.<sup>10–14</sup> For example, Miao *et al.* successfully synthesized a semiconductive Cu-S-MOF with an  $\text{RL}_{\min}$  value of  $-52.8$  dB and an EAB of 6.72 GHz.<sup>13</sup> The conductive Cu-HHTP with a nanorod-like structure that was reported by Zhang *et al.* has an  $\text{RL}_{\min}$  value of  $-63.55$  dB.<sup>15</sup> The controllable chemical composition and morphological structures of cMOFs play an important role in EMW absorption performance.<sup>16</sup> On the one hand, bridging ligands with conjugate systems and metal nodes with various valence states can act as polarization sites to provide dipole polarization loss.<sup>17</sup> On the other hand, the special morphology of cMOFs can provide multiple channels for scattering and reflection, causing some amount of interface polarization loss.<sup>10</sup> Unfortunately, it is still difficult to regulate the conductivity and morphology of cMOFs and then to achieve excellent EMW properties, owing to the complexity and unpredictability of deprotonation and redox reactions of polydentate ligands with high  $\pi$ -conjugation, as well as coordination modes between metal

College of Chemistry and Chemical Engineering, Inner Mongolia University, Hohhot 010021, P.R. China. E-mail: [cezlliu@imu.edu.cn](mailto:cezlliu@imu.edu.cn)

† Electronic supplementary information (ESI) available. See DOI: <https://doi.org/10.1039/d5dt00967g>

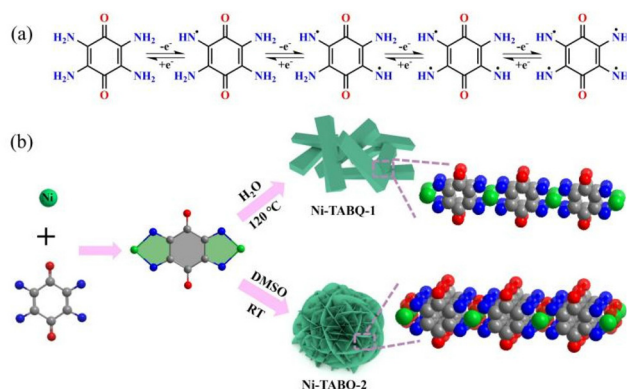


Fig. 1 Synthesis route of Ni-TABQ cMOFs.

centers and bridging ligands in the self-assembly process.<sup>18</sup> Therefore, the fabrication and development of cMOFs with regulated conductivity or microstructure can provide potential reference opportunities for effective EMW absorption materials.

2,3,5,6-Tetraaminobenzoquinone (TABQ) with strong  $\pi$ -conjugated systems, as a redox-activity ligand, may generate *in situ* redox reactions by simultaneous deprotonation, leading to the bidentate functional groups of ligands that may display various chemical valence states under certain conditions (Fig. 1a).<sup>18–20</sup> Herein, two Ni-TABQ cMOFs assembled from TABQ as a bridging ligand and nickel were successfully prepared in different solvent environments, while obviously different microstructures due to the manipulation of the reaction environment. Then, the EMW absorption performance of Ni-TABQ cMOFs was studied systematically. The synergistic effect between the intrinsic conductivity of the obtained Ni-TABQ-1 and bulk morphology optimizes electromagnetic parameters, provides abundant conduction loss and polarization loss, and displays excellent EMW absorption performance, with an  $RL_{\min}$  value of  $-62.68$  dB at 10.16 GHz at a thickness of 2.94 mm and EAB reaching 5.12 GHz at 2.5 mm. This work may provide a simple and useful reference for designing conductive MOFs with superior EMW absorption performance.

## Experimental

### Materials and reagents

Tetrachloro-1,4-benzoquinone ( $C_6Cl_4O_2$ , 98%), phthalimide potassium salt ( $C_8H_4KNO_2$ , 99%), nickel acetate tetrahydrate ( $Ni(OAc)_2 \cdot 4H_2O$ ), nickel nitrate hexahydrate ( $Ni(NO_3)_2 \cdot 6H_2O$ ), aqueous ammonia solution ( $NH_3 \cdot H_2O$ , 25%), hydrazine ( $N_2H_4$ , 50%), hydrochloric acid (HCl, 4 M), *N,N*-dimethyl formamide (DMF, 99%), ethanol (EtOH, 99%), methanol (MeOH, 99%), acetonitrile ( $C_2H_3N$ , 99%) and dimethyl sulfoxide (DMSO, 99%) were used in the experiments and were obtained from commercial sources without further purification. Deionized water ( $H_2O$ ) was generated by a laboratory purification system and utilized in the studies.

### Synthesis of Ni-TABQ-1

According to previously reported literature,<sup>21</sup> TABQ (0.060 g, 0.357 mmol),  $Ni(OAc)_2 \cdot 4H_2O$  (0.132 g, 0.530 mmol),  $H_2O$  (1.5 mL) and  $NH_3 \cdot H_2O$  (7.2 mL) were added to a pressure tube and then the tube was screwed tightly and moved to an oven at 120 °C for 48 h. A black crystalline powder was obtained by filtration after cooling to room temperature, followed by washing with a large amount of  $H_2O$  and MeOH, and then drying at room temperature for at least 24 h.

### Synthesis of Ni-TABQ-2

According to previously reported literature,<sup>22</sup>  $Ni(NO_3)_2 \cdot 6H_2O$  (0.097 g, 0.033 mmol) and  $NH_3 \cdot H_2O$  (1.0 mL) were dissolved in 10.0 mL DMSO to obtain solution A. Under vigorous stirring, solution A was gradually added to solution B which was obtained by dissolving TABQ (0.056 g, 0.033 mmol) in 10.0 mL DMSO drop by drop, and then continued to stir for 3 h. The resultant black powder was filtered under decreased pressure, washed with  $H_2O$ , acetone, and EtOH until the filtrate was colorless, and then dried in a vacuum at 60 °C.

### Characterization

The microstructure of the obtained MOFs was characterized by scanning electron microscopy (SEM, HITACHI S-4800, Japan). Fourier transform infrared (FT-IR) spectroscopy was used for analysing the chemical bonds of the samples. The crystal structure of the as-prepared MOFs was characterized by powder X-ray diffraction (PXRD, Empyrean Panalytical, 40 kV, 40 mA) in the range of 5–50° with Cu K $\alpha$  radiation. The thermal stability measurements were performed under an air atmosphere with a heating rate of 20 °C min<sup>-1</sup> from room temperature to 800 °C using a simultaneous thermal analyzer (HITACHI STA200). Using the Brunauer–Emmett–Teller (BET) method (Quantachrome Autosorb-iQ), which is based on nitrogen adsorption branches recorded at 77 K, the surface area and porosity were examined. Before the BET measurements, the samples were degassed at 120 °C for 8 h. The surface chemical composition of the samples was assessed using X-ray photoelectron spectroscopy (XPS, SMART APEX II) with 284.8 eV as the line position of amorphous carbon. The conductivities of the as-prepared samples were measured using a four-point probe instrument. The as-prepared samples were uniformly mixed with paraffin (the mass ratio is 4 : 6) and pressed into a coaxial ring with an outer diameter of 7.0 mm and an inner diameter of 3.04 mm. The electromagnetic parameters ( $\epsilon_r = \epsilon' + j\epsilon''$ ;  $\mu_r = \mu' + j\mu''$ ) of the samples were determined using a vector network analyzer (VNA, Agilent PNA-N5244A, USA) at 2–18 GHz. The CST Microwave Studio was used to simulate the radar cross-section (RCS) value of the as-prepared samples.

## Results and discussion

The TABQ ligand with a strong  $\pi$ -conjugated system was synthesized by a two-part coupling reaction.<sup>23,24</sup> Then, two Ni-

TABQ cMOFs with different microstructures were synthesized using TABQ and  $\text{Ni}^{2+}$  through the manipulation of the reaction environment during self-assembly (Fig. 1b). As shown in Fig. 2a, the FT-IR spectra further demonstrate that the  $-\text{NH}_2$  of the TABQ ligand deprotonates to generate  $-\text{NH}-$  in alkaline environments, and the N atom in the ligand coordinates with  $\text{Ni}^{2+}$  ions to form a quadrangular  $\pi-\pi/\pi-d$  conjugated structure.<sup>25</sup> Specifically, the stretching band of  $-\text{NH}_2$  disappears at  $3000\text{--}3500\text{ cm}^{-1}$ , and the characteristic absorption peak of  $-\text{NH}-$  appears at  $3250\text{ cm}^{-1}$ . The peaks at  $1618$  and  $1420\text{ cm}^{-1}$  are attributed to the  $\text{C}=\text{N}$  and  $\text{C}-\text{N}$  bonds.<sup>26</sup> Besides, the peak at  $\sim 3405\text{ cm}^{-1}$  in Ni-TABQ cMOFs can be attributed to the O-H stretching band. The thermogravimetric (TG) curves of the two Ni-TABQ MOFs showed a similar change trend, and the skeleton structure of Ni-TABQ MOFs began to break down at approximately  $350^\circ\text{C}$  (Fig. S2a and b, ESI†). Within the range of  $30\text{--}150^\circ\text{C}$ , the weight loss rate of Ni-TABQ-1 is about 3.1%, which might be due to the possible presence of adsorbed water in the framework of Ni-TABQ-1. However, within the same temperature range, the weight loss rate of Ni-TABQ-2 is approximately 6.3%, further proving that in addition to the presence of adsorbed water in Ni-TABQ-2, there might also be the existence of bridging water molecules. This suggests that the primary microstructure difference between Ni-TABQ-1 and Ni-TABQ-2 is based on the presence or absence of bridging water molecules. By causing the bridging water molecules to cross-distribute, Ni-TABQ-2 increases the stacking distance between the layers by interfering with the donor-acceptor interaction between the ligand oxidation chains.<sup>21,22</sup> The crystal structure of Ni-TABQ cMOFs was examined by PXRD (Fig. 2b), and the as-synthesized Ni-TABQ cMOFs were found to possess great crystallinity and purity, which are in good agreement with the simulated spectra that have been published.<sup>21,22</sup> In addition, the PXRD diffraction peaks of Ni-TABQ-1 are sharper than those of Ni-TABQ-2, indicating that the synthesized Ni-TABQ-1 sample has higher crystallinity. The

Ni-TABQ cMOFs were used for the BET test (Fig. S2c, ESI†), displaying a typical type IV isotherm, demonstrating that the composite material had mesoporous properties.<sup>27</sup> As shown in Fig. 2c and d, it can be clearly observed that the difference in the microstructure may be due to the manipulation of the reaction environment. The obtained Ni-TABQ-1 has an observable bulk microstructure in the aqueous solvent system, while the as-synthesized Ni-TABQ-2 shows flower-like morphological structures when DMSO is used as the reaction solvent.

The chemical components and valence states of the samples were characterized by XPS, displaying the existence of C, N, O, and Ni elements in Ni-TABQ (Fig. S2d, ESI†). In the high-resolution C 1s spectrum, the characteristic peaks at 284.8, 285.6, 286.7, and 288.5 eV are attributed to  $\text{C}-\text{C}/\text{C}=\text{C}$ ,  $\text{C}-\text{N}$ ,  $\text{C}=\text{N}$ , and  $\text{C}=\text{O}$ , respectively (Fig. 3a).<sup>26,28</sup> As shown in Fig. 3b, the peaks at 530.9 and 532.5 eV correspond to obvious carbonyl diffraction peaks, such as  $\text{C}=\text{O}$  and  $\text{C}-\text{O}$  in quinone, respectively, indicating that the O atom of the bridging ligand failed to participate in the coordination process with the transition metal. In contrast, the novel signal at 535.4 eV can be ascribed to O-H in water molecules, which further indicates the presence of interlayer water molecules in Ni-TABQ-2.<sup>21,29,30</sup> In the N 1s spectrum, the characteristic peaks at 398.3 and 399.5 eV are attributed to imine  $\text{C}=\text{N}$  and amine  $\text{C}-\text{N}$ , respectively. Furthermore, the peak at 401.2 eV belongs to  $-\text{NH}_2$  (Fig. 3c).<sup>31,32</sup> In the Ni 2p spectrum (Fig. 3d), it can be clearly observed that there are four characteristic peaks. Specifically, the peaks at 855.4 and 872.7 eV are attributed to  $2p_{3/2}$  and  $2p_{1/2}$  of  $\text{Ni}^{2+}$ , and 863.2 and 881.7 eV are satellite peaks of  $\text{Ni}^{2+}$ , respectively, which further proves that  $\text{Ni}^{2+}$  coordinates with the N atom in the ligand.<sup>33</sup>

It is commonly recognized that the real part of the ( $\epsilon'$ ,  $\mu'$ ) electromagnetic parameter indicates the ability to store electrical and magnetic energy, whereas the imaginary part of ( $\epsilon''$ ,  $\mu''$ )

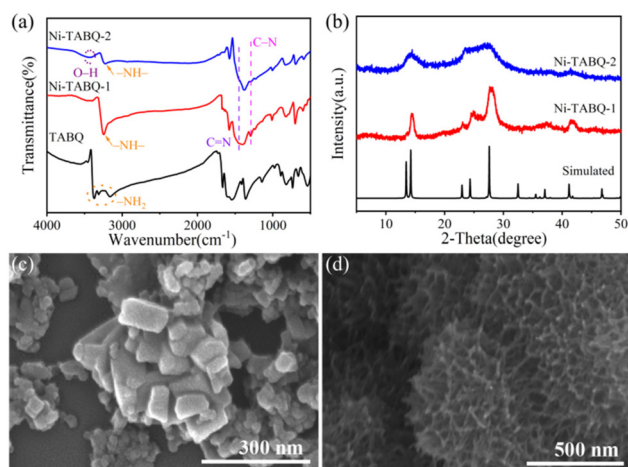


**Fig. 2** (a) FT-IR spectra and (b) the XRD patterns of the obtained Ni-TABQ cMOFs, and SEM images of (c) Ni-TABQ-1 and (d) Ni-TABQ-2.

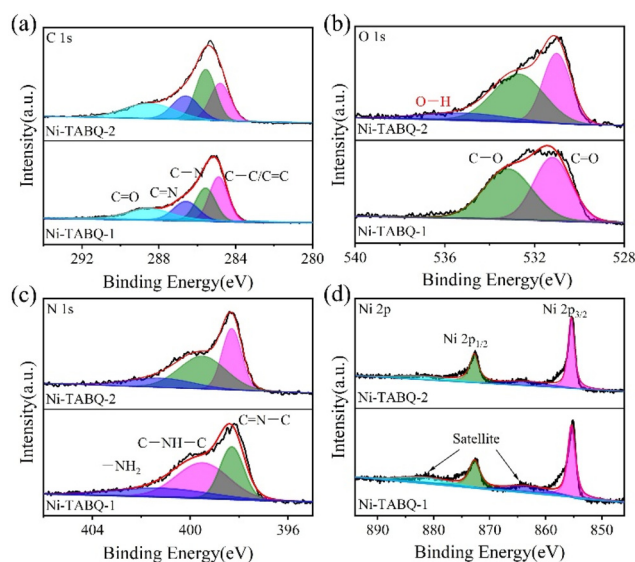


**Fig. 3** High-resolution element spectra of the Ni-TABQ cMOFs: (a) C 1s, (b) O 1s, (c) N 1s, and (d) Ni 2p.

represents the capacity to eliminate energy.<sup>34,35</sup> For examining the EMW absorption characteristics of the Ni-TABQ cMOFs, the electromagnetic parameters were measured over 2–18 GHz, as shown in Fig. 4a–c and Fig. S3 (ESI†). Generally, due to the non-magnetic properties of cMOFs, the  $\mu'$  and  $\mu''$  values of Ni-TABQ cMOFs remain at 1 and 0, respectively, indicating that the absorber has a low magnetic energy storage and dissipation capacity (Fig. S3a and b, ESI†), which can be negligible.<sup>36,37</sup> It is clearly seen that the  $\epsilon'$  and  $\epsilon''$  values of the Ni-TABQ decrease with increasing frequency, which can be attributed to the frequency dispersion effect, where the spin motion of the polar molecule at the GHz frequency is not fast enough to reach equilibrium with the applied electric field, causing the dielectric constant to decrease with increasing frequency.<sup>38,39</sup> According to the free electron theory, the imaginary part of the complex dielectric constant is directly proportional to the electrical conductivity of the absorbers.<sup>35,40</sup>

The electronic conductivity of Ni-TABQ cMOFs was characterized by the four-probe method (Fig. 4d). The conductivity of Ni-TABQ-1 was calculated to be  $1.6 \times 10^{-2} \text{ S cm}^{-1}$ , which may be attributed to the oxidation–reduction of *p*-benzoquinone to hydroquinone by water molecules during the reaction heating process, facilitating charge transfer between the ligand centers and  $\pi$ – $\pi^*$  excitation.<sup>41</sup> However, the conductivity of Ni-TABQ-2 ( $3.0 \times 10^{-4} \text{ S cm}^{-1}$ ) is significantly poorer than that of Ni-TABQ-1. The low conductivity may make the conductive network of the absorber develop abnormally, which is not conducive to impedance matching, resulting in a low dielectric constant for Ni-TABQ-2.<sup>42</sup> More specifically, the  $\epsilon'$  values reduce from 10.66 to 5.70 and 4.85 to 3.99, while the  $\epsilon''$  values decrease from 4.17 to 2.79 and 1.30 to 0.57, respectively (Fig. 4a and b). In addition, the loss tangent value ( $\tan \delta\epsilon$ ;  $\tan \delta\mu$ ) plays a critical role in assessing the main mechanism by which electromagnetic wave energy is converted to another

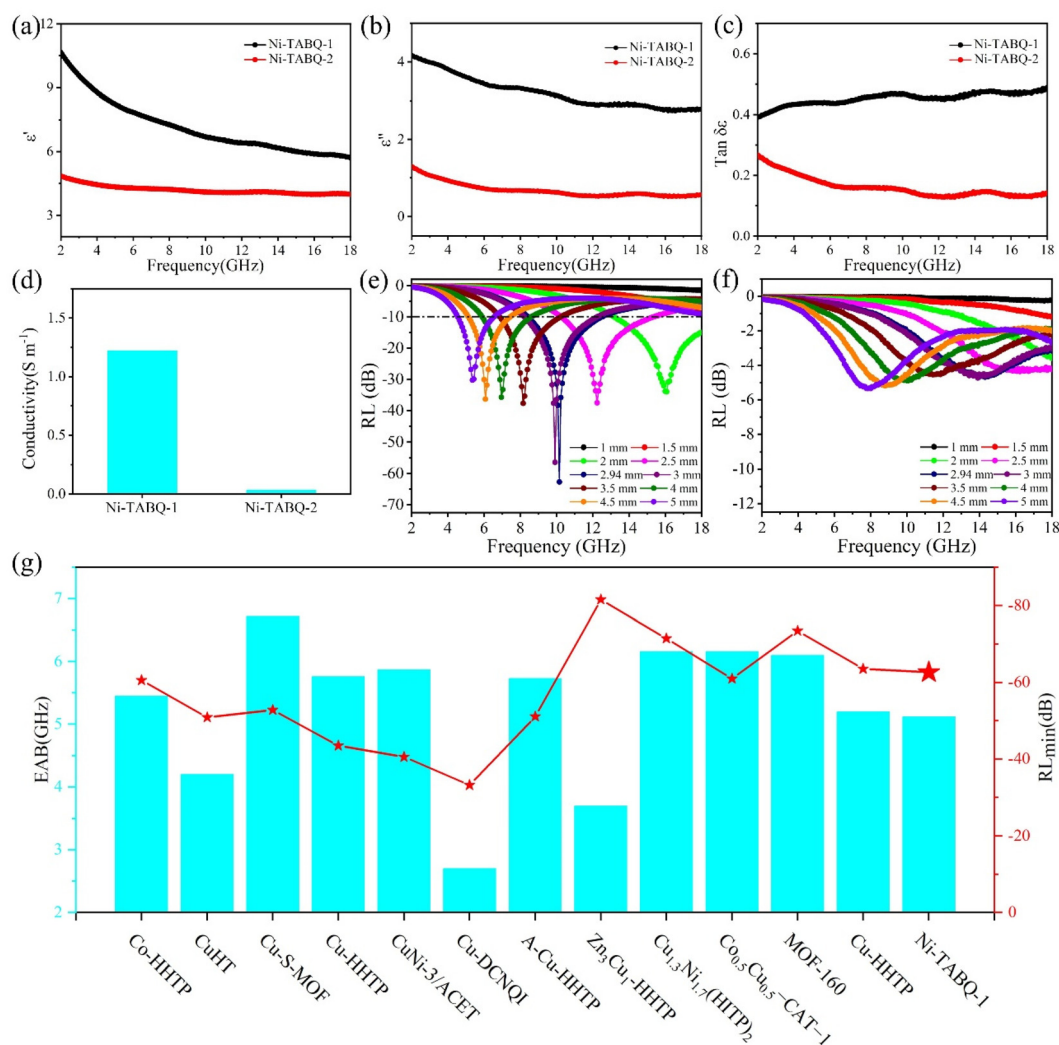


**Fig. 4** Frequency dependence of electromagnetic parameters of Ni-TABQ: (a)  $\epsilon'$ , (b)  $\epsilon''$ , (c)  $\tan \delta\epsilon$ ; (d) the conductivity of Ni-TABQ cMOFs; the RL curves with different thicknesses of (e) Ni-TABQ-1, (f) Ni-TABQ-2, and (g) the  $RL_{\min}$  and EAB of similar conductive MOF-based EMW absorption materials previously reported, whose detailed data are included in Table S1.†



form of energy.<sup>43</sup> The  $\tan \delta\epsilon$  value of the Ni-TABQ cMOFs is much higher than the  $\tan \delta\mu$  value, indicating that it mainly achieves the purpose of attenuating electromagnetic waves through dielectric loss (Fig. 4c and Fig. S3c, ESI†).<sup>44</sup>

The EMW absorption performance of absorbers is often assessed by the RL value, in accordance with the transmission line theory. When the RL value is less than  $-10$  dB, it means that 90% of the incident EMW is absorbed, and a value less than  $-20$  dB means that 99% of the incident EMW is absorbed.<sup>45</sup> The RL value of Ni-TABQ-2 is greater than  $-10$  dB in 2–18 GHz, which shows poor EMW absorption ability (Fig. 4f and Fig. S3b, ESI†). In contrast, Ni-TABQ-1 has effective EMW absorption performance. In particular, the optimal  $RL_{\min}$  value can reach  $-62.68$  dB at 10.16 GHz with a thickness of 2.94 mm, and the EAB is 5.12 GHz (10.24–15.36) at 2.50 mm (Fig. 4e and Fig. S4a, ESI†). Furthermore, Table S1† summarizes a series of conductive MOF-based absorbers in recently published literature studies. By comparing the filling ratio, reflection loss value, absorption bandwidth, and so on, the obtained Ni-TABQ-1 has a relatively strong absorption capacity and a relatively thin thickness, indicating that the obtained Ni-TABQ-1 is a potential absorbent with light weight and effective absorption performance, suggesting that the obtained Ni-TABQ-1 can be regarded as a potential absorption material with light weight and effective absorption performance (Fig. 4g).

Impedance matching ( $|Z_{\text{in}}/Z_0|$ ) and attenuation constant ( $\alpha$ ) play a key role in evaluating the performance of absorbers. Practically, an appropriate  $|Z_{\text{in}}/Z_0|$  value ( $0.8 < |Z_{\text{in}}/Z_0| < 1.2$ ) indicates that EMW are more likely to reach the interior of the absorber than to reflect as little as possible from its surface.<sup>46–48</sup> Compared with Ni-TABQ-2, the optimal frequency of the  $RL_{\min}$  of Ni-TABQ-1 is approximately in the range of well-matched  $|Z_{\text{in}}/Z_0|$ , indicating that a large number of EMW can enter the interior of samples (Fig. S4c and d, ESI†). At the same thickness (2.94 mm), the  $|Z_{\text{in}}/Z_0|$  value of Ni-TABQ-1 is closest to 1, indicating that it has the optimized impedance matching at this thickness, and the EMW is easier to enter the inside of Ni-TABQ-1.<sup>49</sup> The  $\alpha$  values are necessary to assess the ability of the absorber to attenuate electromagnetic energy. The obtained Ni-TABQ-1 has superior EMW attenuation capabilities throughout the whole frequency range, as evidenced by their higher  $\alpha$  values than that of Ni-TABQ-2 (Fig. S5, ESI†).

In order to further analyze the dielectric loss of Ni-TABQ cMOFs, the Cole–Cole curves are drawn according to Debye theory. Typically, each semicircle represents a relaxation behavior in the curves, as shown in Fig. S6a and b (ESI†). It can be observed that at least one semicircle appears in all Ni-TABQ cMOFs, indicating the existence of the Debye relaxation process, which can be attributed to the inevitable interfacial polarization caused by the contact between the massive structures of Ni-TABQ and the presence of a large number of unsaturated bonds and polar functional groups (for example, C=O in benzodione, C=N in the imine structure, and C–N in the amine structure) in Ni-TABQ, resulting in the formation of dipoles and the induction of dipole polarization.<sup>50,51</sup> Besides, there is a straight line extending to the upper right at the end

of the Cole–Cole curve, indicating the presence of conduction losses in all Ni-TABQ cMOFs, which is primarily responsible for the loss in the high-frequency area. This phenomenon can be attributed to the suitable intrinsic conductivity of Ni-TABQ-1, indicating that free electrons can transfer and jump along the  $\pi$ -d conjugated chemical bond plane structure of Ni-TABQ, which is composed of the redox-active TABQ ligand and metal centers under an electromagnetic field. At the same time, the bulk microstructures of Ni-TABQ contact each other to generate micro-capacitance caused by anisotropy and form local conductive networks, providing transport channels for free electrons.<sup>51,52</sup> According to Debye relaxation theory, dielectric loss can be further divided into conductive loss ( $\epsilon''$ ) and polarization loss ( $\epsilon''_p$ ).<sup>53–55</sup> The  $\epsilon''$  of Ni-TABQ-1 decreases with the increase of frequency, while the  $\epsilon''$  of Ni-TABQ-2 changes little with frequency due to low conductivity (Fig. S6c, ESI†). The  $\epsilon''_p$  of all samples showed an obvious trend of fluctuation with the increase of frequency, and the decrease was small (Fig. S6d, ESI†). By comparing  $\epsilon''$  and  $\epsilon''_p$ , it can be inferred that polarization loss plays a major role in the dielectric loss mechanism of all samples.

Moreover, the relationship between the absorber thickness and RL peak frequency is determined by the quarter-wave-length ( $1/4\lambda$ ) matching model. This is satisfied, as the corresponding frequency position of the optimum  $RL_{\min}$  will shift to a lower frequency as the absorber thickness increases. The corresponding frequency of the optimal  $RL_{\min}$  location will shift to a lower frequency as the thickness of the obtained Ni-TABQ-1 increases, satisfying the theoretical model (Fig. S7, ESI†).<sup>48</sup> When the experimental thickness ( $\star$ ) of the optimal  $RL_{\min}$  is consistent with the theoretical thickness, it indicates an interference-type loss.<sup>56</sup>

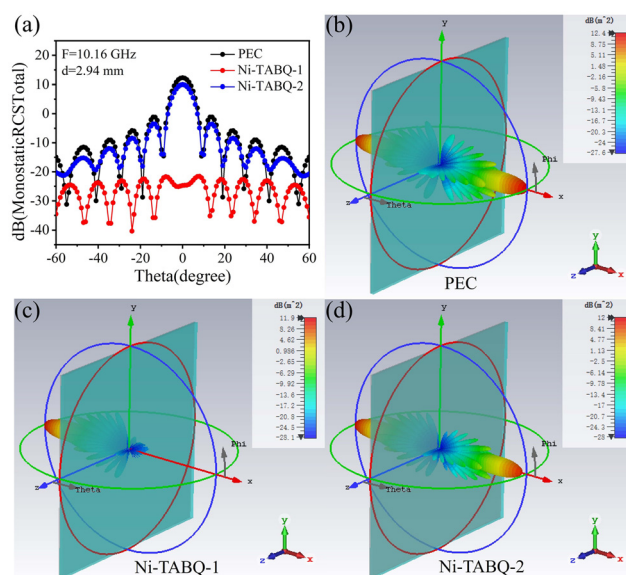


**Fig. 5** (a) The RCS simulation curves at different scanning angles, and 3D radar wave scattering signals of (b) PEC, (c) Ni-TABQ-1, and (d) Ni-TABQ-2.

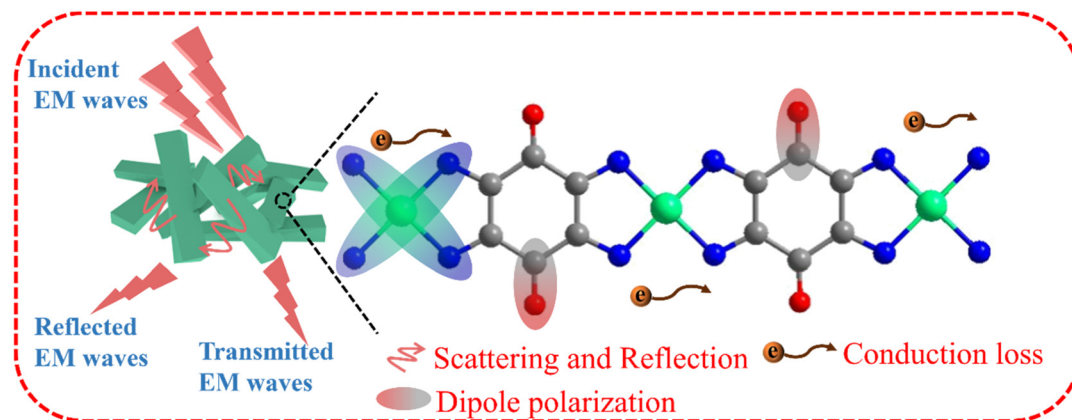


Fig. 6 Summarized mechanism of EMW absorption in Ni-TABQ-1.

EMW absorption materials are often employed as substance coatings in practical applications.<sup>57,58</sup> The radar cross-sectional (RCS) simulation results are shown in Fig. 5 (Fig. S8, ESI†). The resonance intensity of the perfect electrical conductor (PEC) that was coated by the absorber is lower than the pure PEC at vertical incidence. The RCS values of PEC, Ni-TABQ-1, and Ni-TABQ-2 are 12.29, −24.72, and 9.96, respectively. It is important that the RCS values of Ni-TABQ-1 are less than −20 dBm<sup>2</sup> in the −60°–60° range, suggesting that Ni-TABQ-1 can effectively reduce the intensity of PEC metal plate radar scattering, exhibiting excellent stealth performance. Moreover, the scattered signal intensity was in the order of PEC > Ni-TABQ-2 > Ni-TABQ-1. The signal intensity of the pure PEC is stronger than that of the PEC that was coated by Ni-TABQ-1, indicating that the obtained Ni-TABQ-1 has significant EMW absorption performance under real far-field conditions, which can be regarded as a potential stealth material.

Based on the above analysis, the potential EMW absorption processes of Ni-TABQ-1 may be proposed, as shown in Fig. 6. First, the incident EMW may enter the absorber more easily due to the good impedance matching, avoiding the majority of the incident EMW being reflected into free space. Second, the bulk-like morphology of Ni-TABQ-1 not only serves as a possible reflection and scattering channel for electromagnetic waves but also generates micro-capacitance *via* contact with each other to form a local conductive network, allowing free electrons to be transmitted and jumped.

Additionally, Ni-TABQ-1 has rich chemical bonds with  $\pi$ -d conjugation, allowing free electrons to transport and jump within the plane structure of chemical bonds to provide efficient conductive losses. Finally, the large amount of unsaturated bonds and polar functional groups in Ni-TABQ-1, as well as the interface between the MOF, pores, air, and MOF/free space, and micro-capacitors can also act as polarization sites to induce polarization loss. The synergistic action of various loss mechanisms has achieved the purpose of attenuation of EMW. The synergistic effect between the intrinsic conductivity and the bulk-like morphology structure of Ni-TABQ-1

optimizes the electromagnetic parameters to achieve the purpose of EMW attenuation.

## Conclusions

In summary, two Ni-TABQ cMOFs with distinctly different morphologies and conductivities were synthesized by assembling simple and easy-to-make TABQ ligands and Ni<sup>2+</sup> ions through the manipulation of the reaction environment. Then, the EMW absorption performance of Ni-TABQ was studied systematically. More specifically, the obtained Ni-TABQ-1 has relatively higher electrical conductivity and regular bulk-like microstructure, tuning electromagnetic parameters and optimizing impedance matching, resulting in it displaying excellent EMW absorption performance including an RL<sub>min</sub> of −62.68 dB and an EAB of 5.12 GHz. This result proves that the regulation of the microstructure of cMOFs, which may lead to the significantly different electrical conductivity of samples, can be a crucial factor in regulating high-performance EMW absorption, and further provides a reliable reference guide for designing and improving cMOFs with efficient EMW absorption performance.

## Author contributions

Xueling Wang: writing – original draft, writing – review & editing, formal analysis, data curation, investigation, and validation. Xuan Zhang: writing – review & editing and data curation. Jiaqi Lu: writing – review & editing and data curation. Zhiliang Liu: writing – review & editing, conceptualization, funding acquisition, resources, supervision, and project administration.

## Conflicts of interest

There are no conflicts to declare.

## Data availability

All data for this article are either included in the manuscript and its ESI† or are available upon request.

## Acknowledgements

We are grateful for the financial support provided by the NSFC of China (22261038).

## References

- B. Du, D. Zhang, J. Qian, M. Cai, C. He, P. Zhou and A. Shui, *Adv. Compos. Hybrid Mater.*, 2021, **4**, 1281–1291.
- H. Xu, M. Liu, Z. Ma, B. Kang, X. Zhang, C. Zhu, X. Zhang and Y. Chen, *Chem. Eng. J.*, 2024, **479**, 147666.
- R. Li, F. Zhai, Y. Liu, Q. Wang, H. Wei, W. Wu, C. Zhang and W. Chen, *Synth. Met.*, 2024, **301**, 117514.
- H. Lv, J. Cui, B. Li, M. Yuan, J. Liu and R. Che, *Adv. Funct. Mater.*, 2024, 2315722.
- X. Xiong, H. Zhang, H. Lv, L. Yang, G. Liang, J. Zhang, Y. Lai, H.-W. Cheng and R. Che, *Carbon*, 2024, **219**, 118834.
- Y. Wu, D. Lan, J. Ren and S. Zhang, *Mater. Today Phys.*, 2023, **36**, 101178.
- Y. Ye, L. Gong, S. Xiang, Z. Zhang and B. Chen, *Adv. Mater.*, 2020, **32**, 1907090.
- H.-L. Jia, B.-X. Han and G. Li, *J. Solid State Chem.*, 2023, **327**, 124268.
- H. Zhao, F. Wang, L. Cui, X. Xu, X. Han and Y. Du, *Nano-Micro Lett.*, 2021, **13**, 208.
- P. Miao, J. Chen, J. Chen, J. Kong and K.-J. Chen, *Chin. J. Chem.*, 2023, **41**, 1080–1098.
- L. S. Xie, G. Skorupskii and M. Dincă, *Chem. Rev.*, 2020, **120**, 8536–8580.
- M. Majumder, M. S. Santosh, R. Viswanatha, A. K. Thakur, D. P. Dubal and K. Jayaramulu, *Energy Storage Mater.*, 2021, **37**, 396–416.
- P. Miao, N. Qu, W. Chen, T. Wang, W. Zhao and J. Kong, *Chem. Eng. J.*, 2023, **454**, 140445.
- M. Li, G. Zhang, Y. Shi, H. Zhou, Y. Zhang and H. Pang, *Chemistry*, 2023, **5**, 2441–2475.
- X. Zhang, X.-L. Tian, Y. Qin, J. Qiao, F. Pan, N. Wu, C. Wang, S. Zhao, W. Liu, J. Cui, Z. Qian, M. Zhao, J. Liu and Z. Zeng, *ACS Nano*, 2023, **17**, 12510–12518.
- X. Wang, X. Zhang, A. He, J. Guo and Z. Liu, *Inorg. Chem.*, 2024, **63**, 6948–6956.
- J. Liu, G. Xing and L. Chen, *Acc. Chem. Res.*, 2024, **57**, 1032–1045.
- K. Fan, C. Fu, Y. Chen, C. Zhang, G. Zhang, L. Guan, M. Mao, J. Ma, W. Hu and C. Wang, *Adv. Sci.*, 2023, **10**, 2205760.
- Z. Meng, C. G. Jones, S. Farid, I. U. Khan, H. M. Nelson and K. A. Mirica, *Angew. Chem., Int. Ed.*, 2022, **61**, e202113569.
- Y. Jiang, I. Oh, S. H. Joo, Y.-S. Seo, S. H. Lee, W. K. Seong, Y. J. Kim, J. Hwang, S. K. Kwak, J.-W. Yoo and R. S. Ruoff, *J. Am. Chem. Soc.*, 2020, **142**, 18346–18354.
- T. Chen, J.-H. Dou, L. Yang, C. Sun, J. J. Oppenheim, J. Li and M. Dincă, *J. Am. Chem. Soc.*, 2022, **144**, 5583–5593.
- L. Wang, Y. Ni, X. Hou, L. Chen, F. Li and J. Chen, *Angew. Chem., Int. Ed.*, 2020, **59**, 22126–22131.
- Z. Luo, L. Liu, J. Ning, K. Lei, Y. Lu, F. Li and J. Chen, *Angew. Chem., Int. Ed.*, 2018, **57**, 9443–9446.
- Z. Lin, H.-Y. Shi, L. Lin, X. Yang, W. Wu and X. Sun, *Nat. Commun.*, 2021, **12**, 4424.
- Z. Sang, J. Liu, X. Zhang, L. Yin, F. Hou and J. Liang, *ACS Nano*, 2023, **17**, 3077–3087.
- K. Li, J. Yu, Z. Si, B. Gao, H.-g. Wang and Y. Wang, *Chem. Eng. J.*, 2022, **450**, 138052.
- C. Shi, H. Fu, J. Nie and S. Yao, *J. Electron. Mater.*, 2023, **52**, 1375–1384.
- R. Shi, L. Liu, Y. Lu, C. Wang, Y. Li, L. Li, Z. Yan and J. Chen, *Nat. Commun.*, 2020, **11**, 178.
- D. Pakulski, V. Montes-García, A. Gorczyński, W. Czepa, T. Chudziak, M. Bielejewski, A. Musiał, I. Pérez-Juste, P. Samori and A. Ciesielski, *J. Mater. Chem. A*, 2024, **12**, 440–450.
- J. Liu, Y. Yuan, H. Fang, Y. Xu, W. Sun, S. Chen, Y. Wang and L.-P. Lv, *ACS Appl. Energy Mater.*, 2022, **5**, 8112–8122.
- A. Mohtasebi, T. Chowdhury, L. H. H. Hsu, M. C. Biesinger and P. Kruse, *J. Phys. Chem. C*, 2016, **120**, 29248–29263.
- C. Liang, X. Cai, J. Lin, Y. Chen, Y. Xie and Y. Liu, *ChemPlusChem*, 2024, **89**, e202300620.
- H. Wang, X. Cui, Z. Gao, H. Shi and F. Liu, *J. Phys. Chem. Solids*, 2024, **187**, 111876.
- C. Sun, K.-Y. Zhao, M.-L. Huang, C.-L. Luo, X.-D. Chen and M. Wang, *Nano Res.*, 2024, **17**, 1699–1709.
- X. Gao, L. Zhao and Y. Li, *Coord. Chem. Rev.*, 2024, **498**, 215465.
- K. Cao, Y. Fang, S. Wang, Y. Zhang, J. Wen, J. Chen, R. Zhao and W. Xue, *J. Mater. Sci. Technol.*, 2024, **171**, 101–114.
- H. Xu, G. Zhang, Y. Wang, M. Ning, B. Ouyang, Y. Zhao, Y. Huang and P. Liu, *Nano-Micro Lett.*, 2022, **14**, 102.
- B. Quan, X. Liang, G. Ji, J. Ma, P. Ouyang, H. Gong, G. Xu and Y. Du, *ACS Appl. Mater. Interfaces*, 2017, **9**, 9964–9974.
- Y. Dou, N. Liu, X. Zhang, W. Jiang, X. Jiang and L. Yu, *Chem. Eng. J.*, 2023, **463**, 142398.
- Y. Shi, D. Li, H. Si, Z. Jiang, M. Li and C. Gong, *J. Mater. Sci. Technol.*, 2022, **130**, 249–255.
- J. J. Oppenheim, C.-H. Ho, D. Alezi, J. L. Andrews, T. Chen, B. Dinakar, F. Paesani and M. Dincă, *Chem. Mater.*, 2024, **36**, 3395–3404.
- Z. Mu, G. Wei, H. Zhang, L. Gao, Y. Zhao, S. Tang and G. Ji, *Nano Res.*, 2022, **15**, 7731–7741.
- H. Sun, R. Che, X. You, Y. Jiang, Z. Yang, J. Deng, L. Qiu and H. Peng, *Adv. Mater.*, 2014, **26**, 8120–8125.
- Q. Du, Q. Men, R. Li, Y. Cheng, B. Zhao and R. Che, *Small*, 2022, **18**, 2203609.

- 45 Z. Xu, K. Zhang, Y. Cheng, X. Sun, H. Ren, H. Wei, Q. Wang, L. Wang, Z. Zhang and G. Wang, *Chem. Eng. J.*, 2024, **483**, 149186.
- 46 C. Liu, Y. Tong, C. Liu, J. Liu, H. Sun, Q. Hu, S. Wu, Y. Zhao, J. Li, X. Guo and Y. Feng, *Colloids Surf., A*, 2023, **679**, 132605.
- 47 Y. Hou, Z. Sheng, C. Fu, J. Kong and X. Zhang, *Nat. Commun.*, 2022, **13**, 1227.
- 48 X. Xu, Y. Wang, Y. Yue, C. Wang, Y. Wang and D. Liu, *Composites, Part A*, 2022, **162**, 107138.
- 49 T. Wu, F. Ren, Z. Guo, J. Zhang, X. Hou, Z. Chen, Y. Jin and P. Ren, *J. Alloys Compd.*, 2024, **976**, 172984.
- 50 X. Zhang, X. Tian, N. Wu, S. Zhao, Y. Qin, F. Pan, S. Yue, X. Ma, J. Qiao, W. Xu, W. Liu, J. Liu, M. Zhao, K. Ostrikov and Z. Zeng, *Sci. Adv.*, 2024, **10**, eadl6498.
- 51 M. S. Cao, X. X. Wang, M. Zhang, J. C. Shu, W. Q. Cao, H. J. Yang, X. Y. Fang and J. Yuan, *Adv. Funct. Mater.*, 2019, **29**, 1807398.
- 52 L. Duan, J. Zhou, Z. Xu, Y. Liu, Y. Guo, Y. Wang, X. Yang and Z. Yao, *Ceram. Int.*, 2024, **50**, 1013–1021.
- 53 C. Wu, J. Wang, X. Zhang, L. Kang, X. Cao, Y. Zhang, Y. Niu, Y. Yu, H. Fu, Z. Shen, K. Wu, Z. Yong, J. Zou, B. Wang, Z. Chen, Z. Yang and Q. Li, *Nano-Micro Lett.*, 2022, **15**, 7.
- 54 M. Cao, X. Wang, W. Cao, X. Fang, B. Wen and J. Yuan, *Small*, 2018, **14**, 1800987.
- 55 R. Shu, L. Nie, X. Liu and K. Chen, *J. Mater. Sci. Technol.*, 2024, **190**, 106–116.
- 56 Y. Li, X. Liu, X. Nie, W. Yang, Y. Wang, R. Yu and J. Shui, *Adv. Funct. Mater.*, 2019, **29**, 1807624.
- 57 S. Xu, P. Liao, J. Zhu, Z. Yao, X. Zhang, J. Yuan, C. Rong, X. Liu, Z. Xiong and F. Kuang, *Appl. Surf. Sci.*, 2024, **649**, 159200.
- 58 J. Wang, S. Zhang, Z. Liu, T. Ning, J. Yan, K. Dai, C. Zhai and J. Yun, *J. Colloid Interface Sci.*, 2023, **652**, 2029–2041.